Corner- and edge-mode enhancement of near-field radiative heat transfer

Lei Tang[1], Lívia M. Corrêa[2], Mathieu Francoeur[2,3,*], and Chris Dames[1,*]

[1]Department of Mechanical Engineering, University of California at Berkeley, Berkeley, CA, USA
[2]Department of Mechanical Engineering, University of Utah, Salt Lake City, UT, USA
[3]Department of Mechanical Engineering, McGill University, Montréal, QC, Canada
[*]Corresponding authors: mfrancoeur@mech.utah.edu, cdames@berkeley.edu

Abstract

It is well established that near-field radiative heat transfer (NFRHT) can exceed Planck's blackbody limit[1] by orders of magnitude owing to the tunneling of evanescent electromagnetic frustrated and surface modes[2-4], as has been demonstrated experimentally for NFRHT between two large parallel surfaces[5-7] and between two subwavelength membranes[8,9]. However, while nanostructures can also sustain a much richer variety of localized electromagnetic modes at their corners and edges,[10,11] the contributions of such additional modes to further enhancing NFRHT remain unexplored. Here, we demonstrate both theoretically and experimentally a new physical mechanism of NFRHT mediated by these corner and edge modes, and show it can dominate the NFRHT in the "dual nanoscale regime" in which both the thickness of the emitter and receiver, and their gap spacing, are much smaller than the thermal photon wavelengths. For two coplanar 20 nm thick SiC membranes separated by a 100 nm vacuum gap, the NFRHT coefficient at room temperature is both predicted and measured to be 830 W/m^{2}K, which is 5.5 times larger than that for two infinite SiC surfaces separated by the same gap, and 1400 times larger than the corresponding blackbody limit accounting for the geometric view factor between two coplanar membranes. This enhancement is dominated by the electromagnetic corner and edge modes which account for 81% of the NFRHT between the SiC membranes. These findings are important for future NFRHT applications in thermal management and energy conversion.

The NFRHT between micrometer-[5,6,12,13] and millimeter-scale[7,14-18] parallel flat surfaces and between two subwavelength membranes[8,9] separated by a nanoscale vacuum gap d has been well established to exceed the blackbody limit[1], in agreement with fluctuational electrodynamics predictions[2,3,19,20]. The mechanism responsible for this enhancement is well understood and is mediated by the tunneling of evanescent electromagnetic waves, which include frustrated and surface modes[2-4]. Such near-field enhancements to the heat transfer are expected to become important only when d is much smaller than the characteristic thermal wavelengths of the corresponding free-space photons, λ_{th}.

The physics of NFRHT becomes even richer when the size of the emitter and receiver themselves, for example as characterized by their transverse breadth (membrane thickness t in Fig. 1), is also in the deep subwavelength regime. In this case, the membranes can also sustain localized electromagnetic corner and edge modes which are otherwise forbidden by the translational symmetry of infinite parallel surfaces and play only a negligible role in NFRHT between relatively thick membranes[8,9,21]. Such modes have previously been studied in non-thermal contexts like plasmonic phenomena in nanoscale metal structures[10,11]. Unexplored, however, is the potential for such corner and edge modes to couple across two nanostructures in the near field and thereby contribute to NFRHT.

Here we investigate both theoretically and experimentally the NFRHT in this "dual nanoscale" regime, in which both d and $t << \lambda_{\mathrm{th}}$. As depicted in Fig. 1a, we study the NFRHT between several pairs of coplanar SiC membranes with t and d both much smaller than the relevant $\lambda_{\mathrm{th}} \gtrsim 7$ μm. We find that the new physical mechanism introduced by electromagnetic corner and edge modes leads to large enhancements of NFRHT compared to the case of two infinite parallel surfaces, and

indeed can dominate the NFRHT for $t << d << \lambda_{th}$. For 20 nm thick SiC membranes separated by a vacuum gap of 100 nm, the room temperature radiative heat transfer coefficient h_{rad} = 830 W/m^{2}K, with excellent agreement between theory and measurement. This h_{rad} is very large, being 5.5 times larger than calculated for two infinite SiC surfaces separated by the same gap, and 1400 times larger than the corresponding blackbody limit accounting for the geometric view factor between the emitter and receiver face areas of two coplanar membranes. This large NFRHT in the dual nanoscale regime might be exploited in a variety of applications, such as localized radiative cooling[22], thermal management technologies[23-27], and energy conversion devices[28-32].

Devices for measuring NFRHT

We measure NFRHT in the dual nanoscale regime using three main microfabricated devices consisting of pairs of suspended coplanar SiC membranes with thicknesses of 20, 50, and 120 nm (Fig. 1b). The choice of SiC membrane dimensions was guided by preliminary numerical simulations of NFRHT using the discrete system Green's function (DSGF) method.[33]

Each device consists of two symmetrical islands, the heating island at temperature T_h and the cold island at T_c. Each island is supported by six long suspended beams (Pt on SiNx) and incorporates a serpentine Pt resistance thermometer (PRT) for heating and thermometry. The NFRHT is between the thin symmetrical SiC membranes separated by a nanosized gap d. The length L of all devices is 30 μm, and the suspended portions of the SiC membranes have widths w = 9 μm for the 120 nm thick device and w = 1 μm for the 50 and 20 nm thick devices. Another t = 20 nm, L = 30 μm device was prepared with w = 2 μm.

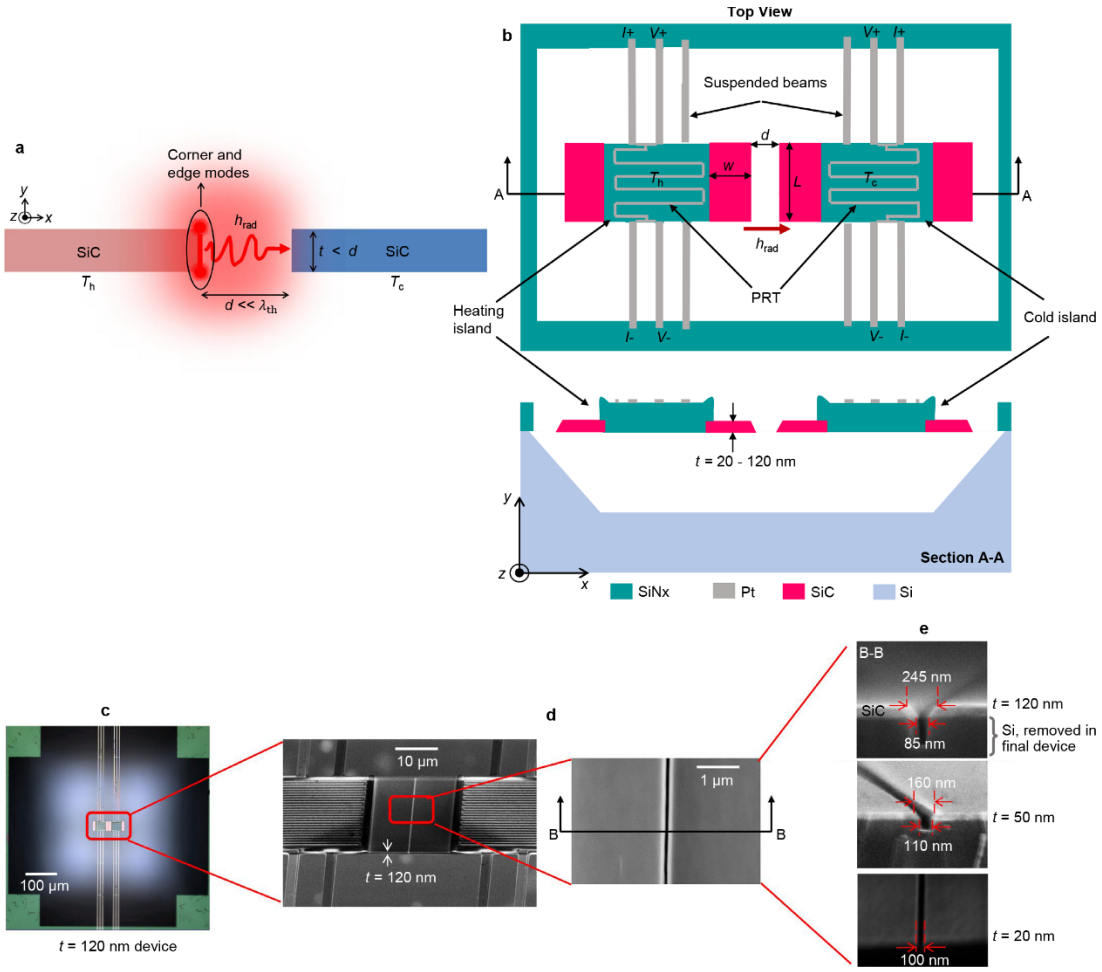

Fig. 1 | Principle of NFRHT in the dual nanoscale regime and a device for measuring it. a, Concept of NFRHT between two thin coplanar SiC membranes mediated by electromagnetic corner and edge modes. **b,** Schematic of the measurement device. Matched SiC membranes separated by a gap d are supported by symmetric SiNx islands, each with a Pt serpentine for Joule heating and resistance thermometry to measure the NFRHT. The three main devices studied in this work use paired SiC membranes with thicknesses $t = 20$, 50, and 120 nm, and average gap spacings of $\bar{d} = 100$, 135, and 165 nm, respectively. **c,** Optical and **d,** SEM images of the released 120 nm thick device. **e,** SEM images of the SiC gap details of the three main devices, after the etch to define the gap but prior to removing the sacrificial Si underlayer. The 20 nm thick device has an approximately uniform gap $\bar{d} = 100$ nm, while the 120 and 50 nm thick devices exhibit sloped gaps with d from 85 nm to 245 nm ($\bar{d} = 165$ nm) and from 110 nm to 160 nm ($\bar{d} = 135$ nm), respectively. Such sloped d is taken into account in the DSGF simulations of Fig. 2 (see also Supplementary Fig. 7).

Two symmetric SiC "wings" are located on each island on the side opposite to the SiC membranes that carry the NFRHT. These wings have the exact same dimensions as the inner SiC membranes, and are included to increase the yield of the devices during release. The SiNx of the islands is patterned to slightly overlap the contact edges of the SiC membranes and wings by ~1 μm to minimize the thermal contact resistance. More details about the microfabrication are given in Supplementary Section 1 and Extended Data Fig. 1, and about the device design in our recent work measuring the thermal conductivity of similar SiC films.[34]

Figure 1(c,d) respectively show optical and scanning electron microscope (SEM) images of the 120 nm thick device. The gap spacing d is estimated from tilted SEM images of the membrane cross-sections prior to the final release step (the KOH release etch of Si has negligible impact on the SiC thickness and the gap spacing after release, see Supplementary Sections 1 and 2). For the two thicker samples, Fig. 1e shows how the SiC etch resulted in sidewalls that are sloped rather than being perfectly vertical. For example, for the 120 nm thick device the gap spacing ranges from 85 nm to 245 nm, with an average gap spacing $\bar{d} = 165$ nm. The DSGF simulations of NFRHT below use this actual sloped gap geometry. Similarly, the 50 nm thick device has a gap sloping from 110 to 160 nm ($\bar{d} = 135$ nm), while both 20 nm thick devices have an approximately uniform gap of $d = \bar{d} = 100$ nm.

The flatness and coplanarity of the suspended SiC membranes after their release is another key consideration, which we characterize using 3D laser confocal microscopy (LCM). For all devices the LCM topography scans confirmed very good alignment of the suspended SiC membrane edges across the gap, with a misalignment of no more than ±20 nm when comparing the y-heights of the left and right SiC membranes' free edges at the gap (see Supplementary Table 1 and Supplementary

Fig. 2). Similarly, LCM was also used to quantify the slight tilt of each suspended $L \times w$ membrane away from its ideal *x*-*z* plane; as expected these tilts were small, never more than 5°, and also quite symmetric about the gap (see Supplementary Sections 3 and 4). Additional DSGF simulations of such residual *y*-misalignment and tilt effects indicate they should have negligible impact on h_{rad} (less than 12%; see Methods).

NFRHT measurement procedure

The NFRHT measurements follow a well-established electrothermal approach[34-38] (see also Supplementary Section 5), in which Joule heating at the hot island creates a small temperature difference across the gap that is measured using resistance thermometry of each island's PRT. AC lock-in methods are used to enhance accuracy, with typical heating current I_f of amplitude 8 μA and frequency f of 0.98 Hz. The resulting temperature rises of both islands at $2f$ are denoted $\Delta T_{\mathrm{h},2f}$ and $\Delta T_{\mathrm{c},2f}$. The typical temperature difference across the gap is $T_{\mathrm{h}} - T_{\mathrm{c}} \sim 1$ K, and measurements are repeated for cryostat stage temperature T ranging from 200 K to 400 K. The cryostat operates at a vacuum level better than 5×10^{-6} torr, such that convection and conduction through residual air are negligible. Finally, the total heat transfer coefficient from the heating island to the cold island is calculated as $h = \frac{G}{Lt}$ where G is the total thermal conductance. For this AC scheme Refs. [35,36] have shown that $G = \frac{\partial Q}{\partial\left(\Delta T_{\mathrm{h},2f}+\Delta T_{\mathrm{c},2f}\right)} \cdot \frac{\partial \Delta T_{\mathrm{c},2f}}{\partial\left(\Delta T_{\mathrm{h},2f}-\Delta T_{\mathrm{c},2f}\right)}$, where Q is the total Joule heating at the heating island's PRT plus one current-carrying Pt lead.

While the experimentally obtained h between hot and cold islands is dominated by the NFRHT across the vacuum gap separating the SiC membranes, this total h is also increased by contributions from any residual parasitic pathways. As detailed in Supplementary Section 6, the corresponding parasitic background conductance $G_{\mathrm{parasitic}}$ was determined experimentally using a series of

matched reference devices, and found to be never more than 35% of the total G, so that in all cases the raw measured G of the test devices is dominated by the NFRHT contribution G_{rad}. Accordingly, the parasitic heat transfers have already been subtracted for all h_{rad} results presented below in Fig. 2, a correction of no more than 35%.

Results

The measured h_{rad} for the three main devices is shown by the solid-colored points in Fig. 2a with the experimental schematics shown in Fig. 2b, and Fig. 2c is a "slice" through those same results at T = 300 K to better highlight the trends with membrane thickness. In both panels of Fig. 2a and 2c, the hollow square point corresponds to the fourth device also with t = 20 nm and d = 100 nm, which was measured only at 300 K as an additional verification. The two 20 nm thick devices are nominally identical except for having two different widths of the suspended SiC membrane: w = 1 μm for the primary device (solid red points in Fig. 2a) and w = 2 μm for the alternate device (hollow red point). Even with their different values of w (and different $G_{parasitic}$), both 20 nm thick devices give nearly the same final value of h_{rad}, within 4%.

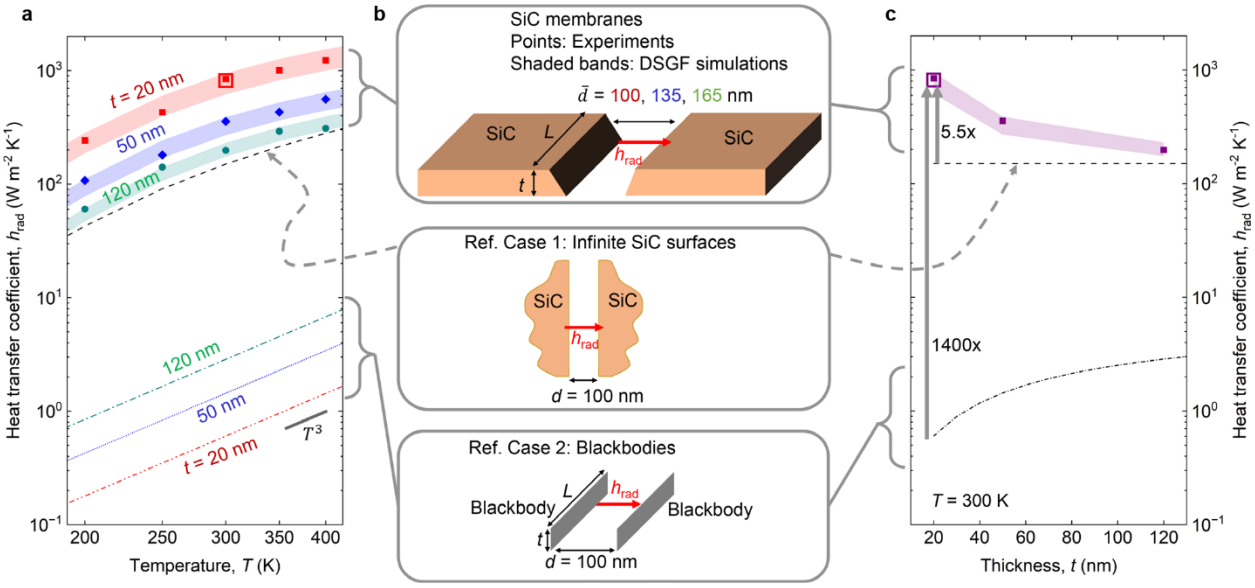

Fig. 2 | Measured and modeled radiative heat transfer coefficients between coplanar SiC membranes. a, Measured (solid-colored points) heat transfer coefficients for the three main devices, denoted by their membrane thicknesses t = 20, 50, and 120 nm, showing very good agreement with the corresponding DSGF simulations with no free parameters (color-coded shaded bands). The hollow red point is from another t = 20 nm, d = 100 nm device, measured only at 300 K. Each experimental point has an estimated h_{rad} uncertainty of ±10% (representing 68% confidence interval), which is similar to the size of the points and has been omitted for visual clarity. The dashed lines are calculations for two reference cases: Ref. Case 1 is the near-field h_{rad} between two infinite SiC surfaces separated by a gap d = 100 nm, and Ref. Case 2 is h_{rad} between parallel blackbody surfaces evaluated using standard view factors corresponding to d = 100 nm and the same L and t values as the three measured devices. **b,** Schematics of the device membrane geometries as well as the two reference cases. **c,** A slice through the data from **a** at 300 K, to better reveal how h_{rad} increases as the membrane thickness t decreases.

The color-coded shaded bands in Fig. 2 depict the corresponding DSGF simulations of h_{rad}. There is very good agreement between theory and experiment across all devices and temperatures. DSGF is a powerful and rigorous numerical approach to calculate the radiation heat transfer between 3D thermal emitters and receivers of arbitrary shapes and sizes based on discretization into cubic subvolumes[33] (see Methods for details). These DSGF simulations have no free parameters, with

the only inputs being the temperature, the frequency-dependent dielectric function of SiC (see Methods), and the geometries of the emitter and receiver membranes. For all devices the finite breadth of the shaded bands of the DSGF predictions reflect the uncertainties arising from the small but finite tilting of the membranes as well as the actual nonuniform gap spacings (sloped d) of the 50 and 120 nm thick devices, as extracted from the LCM measurements and SEM images, respectively (see Methods). More details about the DSGF calculations and convergence are given in Supplementary Section 7.

A remarkable feature of the SiC NFRHT results in Fig. 2 is that h_{rad} increases strongly with decreasing t. For further context, Fig. 2 includes theoretical results for two reference conditions. Reference Case 1 is a standard calculation (see Methods) for NFRHT between two infinite SiC surfaces ($t \to \infty$) separated by a gap of d = 100 nm, chosen to match the smallest d of the experimental devices. At room temperature the measured h_{rad} for the 20 nm thick devices reaches a very large value of 830 W/m^{2}K (average of both 20 nm thick devices), which is 5.5 times larger than the h_{rad} of 150 W/m^{2}K predicted between two infinite surfaces. This 5.5-fold enhancement strikingly demonstrates the impact of additional physics of enhanced NFRHT in the "dual nanoscale" regime of small d and t, as compared to the traditional "single nanoscale" regime of small d alone[5-7,12-18] and the case of thick membranes.[8,9,21]

As a different perspective we can consider the thermal conductance $G_{rad}=h_{rad}Lt$, using h_{rad} from Fig. 2c. For example at room temperature the corresponding experimental G_{rad} values are 0.71, 0.53, and 0.50 nW/K for the samples of t = 120, 50, and 20 nm, respectively. Because the gap spacing d also varies slightly among these samples, we performed additional simulations to isolate the impact of t on G_{rad}, for fixed d = 100 nm (Extended Data Fig. 2).

We further find that the SiC NFRHT in this dual nanoscale regime is dominated by evanescent waves rather than propagating waves (see Supplementary Section 8 and Extended Data Fig. 3). As such, the physical mechanism underlying the heat transfer enhancement displayed in Fig. 2 is entirely different than that reported in Ref. 39, where radiative heat transfer between the subwavelength membranes was in the far-field regime and thus solely mediated by propagating waves.

Reference Case 2 is the blackbody limit in which all near-field and nanoscale effects are neglected. The two islands are treated as blackbodies, configured as parallel aligned rectangles each of area Lt. This leads to $h_{\mathrm{BB}} = 4\sigma_{\mathrm{SB}}T^3F_{12}$, where σ_{SB} is the Stefan-Boltzmann constant and F_{12} is the geometric view factor between the two rectangles[40] (see Methods). Figure 2 shows that the measured NFRHT between SiC membranes in the dual nanoscale regime is vastly larger than the blackbody limit for this idealized geometry. For example, for 20 nm thick membranes separated by d = 100 nm, the measured h_{rad} at room temperature is around 1,400 times larger than the value of 0.61 W/m^{2}K for Reference Case 2. Similarly large enhancements are found for other temperatures (see Supplementary Section 9).

Physical basis of the NFRHT enhancement

The large enhancement of NFRHT in the dual nanoscale regime fundamentally arises from the tunneling of evanescent electromagnetic corner and edge modes between the SiC membranes, a mechanism which is forbidden by symmetry[5-7,12-18] or negligible[8,9,21] in previous works. These modes are generated by the electromagnetic field couplings in the x-y plane. There is no field coupling along the z-direction, because the membrane length L is much larger than the thermal photon wavelengths (practically $L \to \infty$). As such, the emergence of corner and edge modes can

be understood using a 2D structure as shown in Fig. 1a and Fig. 3, consistent with Berini's framework[10,11]. Specifically, in a solitary membrane the evanescent electromagnetic fields in the *x*-*y* plane associated with surface phonon-polaritons (SPhPs) traveling along the *z*-direction couple between the membrane's perpendicular edges through the corners and between the adjacent corners to form four fundamental electromagnetic corner and edge modes[10,11]. Higher order resonances are also supported, but only the fundamental modes are important and therefore considered hereafter.

Figure 3a shows the spectral heat transfer coefficient at 300 K predicted using DSGF, along with a modal analysis of solitary 20, 50 and 120 nm thick SiC membranes in Fig. 3(b,c). The modal analysis is performed with COMSOL Multiphysics, and has been verified against the results of Ref. 11 for a silver membrane (see Supplementary Section 10). The modal analysis is performed on infinitely long ($L \to \infty$), 2D membranes characterized by perfectly straight corners. Similarly, the spectral heat transfer coefficient is calculated for a uniform gap spacing of 100 nm (the calculations were repeated using nonuniform gap spacings, which was found to have almost no impact; see Supplementary Section 11).

For vacuum gap spacings in the deep subwavelength regime like in the present work ($d \ll \lambda_{\mathrm{th}}$), NFRHT between two infinite SiC surfaces is known to be dominated by SPhPs confined to the neighborhood of a single SiC-vacuum interface; these SPhPs can exist only in TM polarization[2,3]. The SPhP resonant frequency of a planar SiC-vacuum interface is estimated to be 1.77×10^{14} rad/s from a SPhP dispersion relation (see Methods), which is in good agreement with the high-frequency peak in the spectral heat transfer coefficient calculated between two infinite surfaces (Fig. 3a). Compared to the case of two infinite surfaces, DSGF calculations of the spectral heat

transfer coefficient in Fig. 3a for nanosize t show that the resonance is redshifted and broadened as the membrane thickness decreases.

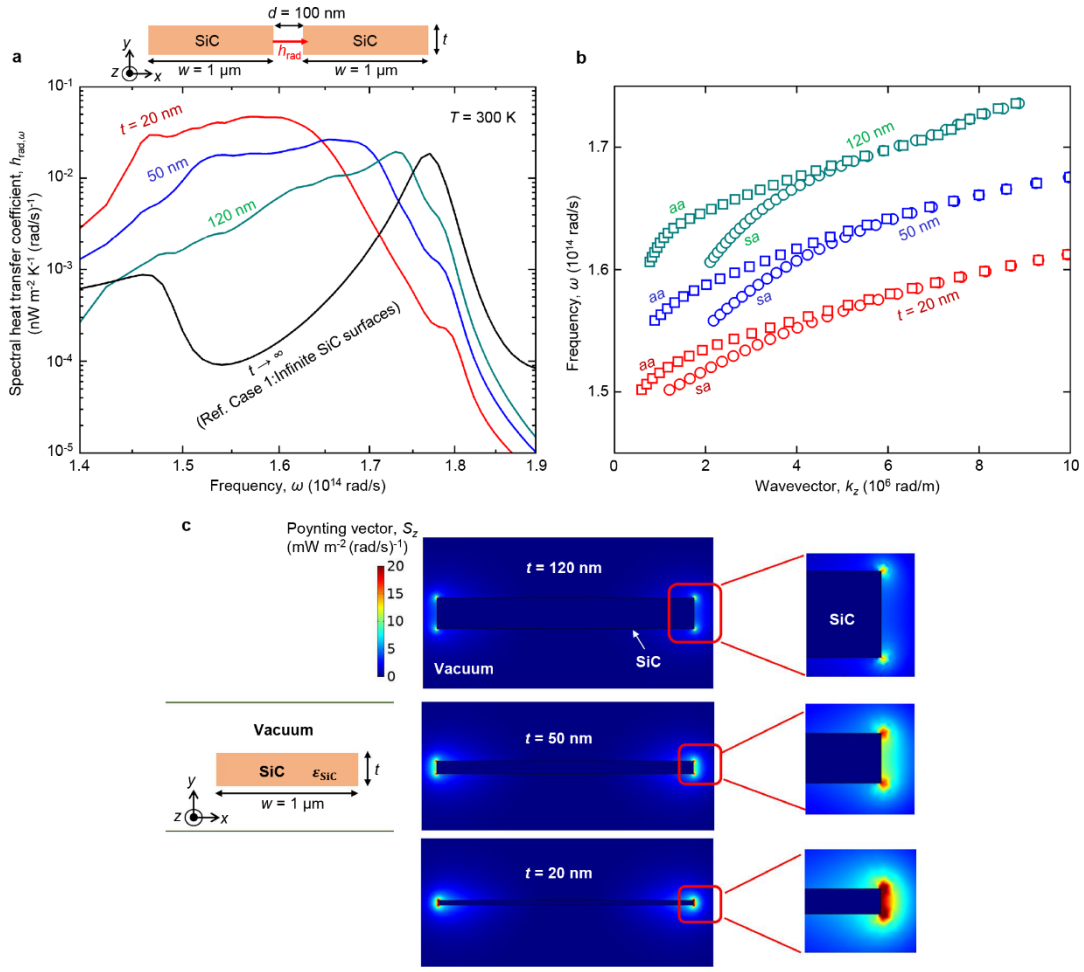

Fig. 3 | Theoretical analysis of NFRHT enhancement mediated by electromagnetic corner and edge modes in the dual nanoscale regime between two coplanar SiC membranes. DSGF simulations are performed on 3D membranes (finite t, w, and L), whereas COMSOL Multiphysics simulations are performed on 2D membranes (equivalent to $L \to \infty$). Both approaches here assume perfectly straight corners. **a,** DSGF calculated spectral heat transfer coefficient $h_{\mathrm{rad},\omega}$ at 300 K for membrane thicknesses of 20, 50, and 120 nm, as well for infinite parallel surfaces, all for a 100 nm gap. As the membrane thickness decreases, the resonance peak of $h_{\mathrm{rad},\omega}$ increases, redshifts, and broadens, which also increases the total NFRHT. **b,** Dispersion relations of the two low-frequency fundamental electromagnetic corner and edge modes, denoted *aa* and *sa* (see main text), in solitary 20, 50, and 120 nm thick membranes calculated with COMSOL Multiphysics. For each thickness, the *aa* and *sa* branches become degenerate with each other above $k_z \sim 5\times10^6$ rad/m. **c,** Poynting vector along the z-direction, S_z, calculated with COMSOL Multiphysics, showing representative electromagnetic corner and edge modes in solitary 20, 50 and 120 nm thick membranes. The Poynting vector of each membrane is evaluated at the frequency ω corresponding to $k_z = 5\times10^6$ rad/m, as determined using the *aa* mode dispersion relations of **b**.

This trend is physically explained by analyzing the electromagnetic corner and edge mode dispersion relations (Fig. 3b), for the angular frequency, ω, as a function of the real component of the wavevector along the z-axis, k_z. The four fundamental corner and edge modes are categorized in terms of the symmetry (s) and asymmetry (a) of the y-component of the electric field with respect to the y and x axes, respectively[11]. Here, we focus on the two low-frequency modes, designated *aa* and *sa*, corresponding to two branches in the dispersion relations, because only these modes are important for the resonances much below the longitudinal optical phonon frequency (1.801×10^{14} rad/s, see Methods); the *as* and *ss* modes are not important in this regime. Further, for every thickness considered, the calculations in Fig. 3b show that for k_z above ~5×10^6 rad/m, the *aa* and *sa* modes become essentially degenerate with each other and merge into a single branch in the dispersion relations. Also, for the 120 nm thick membrane, the dispersion relation reaches a regime of nearly constant ω for $k_z > 9\times10^6$ rad/. This cutoff occurs because the modal analysis is performed using a real frequency ω and thus a complex wavevector k_z. Although this approach cannot be used as a measure of the local density of states[41], it is the resonant frequencies that are of interest here, and additional calculations applying the SiC dielectric function (Eq. 8) to the framework of Ref. 41 show that there is no perceptible impact on estimating the resonant frequencies regardless of whether they are calculated using real ω or real k_z.

The thin-membrane geometries of the present work can sustain much richer electromagnetic modes than traditional infinite surfaces. For example, while the confined SPhPs at a single SiC-vacuum interface are purely TM-polarized, the corner and edge modes in membranes are not, since all six field components exist for all modes[11] (see Supplementary Section 12). In the electrostatic limit (i.e., k_z much larger than the vacuum wavevector, k_0), for polar dielectrics like SiC, the largest contributing wavevector dominating NFRHT is estimated as $k_z \approx d^{-1}$,[42] which for a 100-nm

vacuum gap spacing corresponds to $k_z \approx 1.0\times10^7$ rad/m. Now referring back to Fig. 3b for the corresponding ω, we can expect the spectral $h_{\mathrm{rad},\omega}$ to peak at around 1.61×10^{14}, 1.68×10^{14} and 1.74×10^{14} rad/s for the 20, 50 and 120 nm thick membranes, respectively. Finally, inspection of the actual calculated spectral $h_{\mathrm{rad},\omega}$ curves in Fig 3a confirms that all three do indeed peak at frequencies close to the values deduced from Fig. 3b. This excellent agreement between the resonance predictions of Fig. 3b and the spectral heat transfer coefficient peaks in Fig. 3a, obtained using two entirely different calculations, explains the resonance redshift observed as the membrane thickness decreases. Also, the resonance broadening with decreasing thickness seen in Fig. 3a can be explained by the fact that losses in SiC increase within the Reststrahlen spectral band as the frequency is redshifted (see Supplementary Section 13 for details).

Turning to a representative real space visualization, Fig. 3c shows an example of the z-component of the Poynting vector, S_z, for three different membranes for the *aa* mode at $k_z = 5\times10^6$ rad/m. For the 120 nm thick membrane, this Poynting energy is relatively small and is localized to the corners of the membrane. Then as the membrane thickness decreases the modes couple more strongly in the y-direction, causing S_z to become larger around both the corners and vertical edges, which is what allows these electromagnetic corner and edge modes to dominate NFRHT for the 50 and 20 nm thick membranes. Extended Data Fig. 4 also shows the spatial distribution of power density dissipated between the membranes due to these corner and edge modes.

To quantify the relative contribution of corner and edge modes to the NFRHT, above and beyond the traditional NFRHT between infinite planar surfaces, we introduce a NFRHT enhancement ratio: $R = \frac{h_{\mathrm{rad}}(d,t)}{h_{\mathrm{rad}}(d,t\to\infty)}$, where $h_{\mathrm{rad}}(d,t)$ is for a thin pair of coplanar membranes and $h_{\mathrm{rad}}(d,t\to\infty)$ is

for infinite surfaces at the same gap spacing d. In both cases we assume $L \gg \lambda_{\mathrm{th}}$ so that practically $L \to \infty$.

Calculations for t = 20 nm and a uniform gap d = 100 nm at 300 K yield R = 5.3, indicating that $\frac{R-1}{R} = 81\%$ of the total NFRHT is mediated by the corner and edge modes. Similar calculations for 50 nm thick membranes with a 100-nm gap give R = 3.4, so that corner and edge modes still dominate with a relative contribution of 71%. Finally, calculations for t = 120 nm, d = 100 nm yield R = 1.7, showing that now more than half (59%) of the NFRHT is instead mediated by the SPhPs that already exist in infinite planes (here corresponding to the y-z plane) with their evanescent fields decaying in the x-direction. Clearly, for ever thicker membranes ($t \to \infty$), the relative impact of corner and edge modes must become ever more negligible, eventually reverting to the NFRHT between two infinite plates ($R \to 1$).

In summary, we predicted and measured NFRHT in the dual nanoscale regime between two coplanar SiC membranes with thickness comparable to or smaller than their vacuum gap spacing of ~100 nm for temperatures ranging from 200 to 400 K. The measurements agree very well with theoretical predictions based on the DSGF method and no free parameters. The results demonstrate a novel mechanism mediated by electromagnetic corner and edge modes for enhancing NFRHT well beyond that between two infinite parallel surfaces. These newly-observed resonant modes can dominate the NFRHT with a relative contribution exceeding 80% for the thinnest membranes in this study. The measured radiative heat transfer coefficient at 300 K between 20 nm thick SiC membranes is 830 W/m^{2}K, which is 5.5 and 1400 times larger than that between two infinite SiC planes and between two coplanar blackbody membranes, respectively. The emergence of electromagnetic corner and edge resonant modes in subwavelength membranes opens a new route

for enhancing and spectrally controlling NFRHT. Such high heat transfer could enable future applications of NFRHT in noncontact localized radiative cooling, thermal management, and energy conversion devices.

Methods

DSGF simulations of NFRHT. NFRHT between two SiC membranes separated by a vacuum gap is modeled using the DSGF method[33], which is a numerically exact volume integral formulation based on fluctuational electrodynamics[20]. The DSGF method calculates the unknown system Green's function, $\overline{\overline{\mathbf{G}}}(\mathbf{r}, \mathbf{r}', \omega)$, relating the electric field with frequency ω observed at point $\mathbf{r}$ to a point source excitation at $\mathbf{r}'$. The unknown system Green's function is expressed in terms of the known free-space Green's function, $\overline{\overline{\mathbf{G}}}^0(\mathbf{r}, \mathbf{r}', \omega)$, as follows:

$$\overline{\overline{\mathbf{G}}}^0(\mathbf{r}, \mathbf{r}', \omega) = \overline{\overline{\mathbf{G}}}(\mathbf{r}, \mathbf{r}', \omega) - k_0^2 \int_{V_{\text{therm}}} \overline{\overline{\mathbf{G}}}^0(\mathbf{r}, \mathbf{r}'', \omega)[\varepsilon(\mathbf{r}'', \omega) - 1]\overline{\overline{\mathbf{G}}}(\mathbf{r}'', \mathbf{r}', \omega)\, d^3\mathbf{r}'' \quad (1)$$

where k_0 is the vacuum wavevector magnitude, ε is the dielectric function of SiC, and V_{therm} is the combined total volume of the thermal objects (here, the two membranes). The free-space Green's function in vacuum is calculated as:

$$\overline{\overline{\mathbf{G}}}^0(\mathbf{r}, \mathbf{r}', \omega) = \frac{\exp(ik_0 r)}{4\pi r}\left[\left(1 - \frac{1}{(k_0 r)^2} + \frac{i}{k_0 r}\right)\overline{\overline{\mathbf{I}}} - \left(1 - \frac{3}{(k_0 r)^2} + \frac{3i}{k_0 r}\right)\hat{\mathbf{r}}\hat{\mathbf{r}}^{\dagger}\right] \quad (2)$$

where $r = |\mathbf{r} - \mathbf{r}'|$, $\hat{\mathbf{r}} = \frac{\mathbf{r}-\mathbf{r}'}{|\mathbf{r}-\mathbf{r}'|}$, $\overline{\overline{\mathbf{I}}}$ is the unit dyadic, and † is the conjugate transpose operator. The volume of the thermal objects, V_{therm}, is discretized into N cubic subvolumes along a cubic lattice. From Eq. (1), a system of linear equations of the form $\overline{\overline{\mathbf{A}}}\,\overline{\overline{\mathbf{G}}} = \overline{\overline{\mathbf{G}}}^0$ is derived,[33] where $\overline{\overline{\mathbf{A}}}$ is the $3N \times 3N$ interaction matrix accounting for N subvolumes and three Cartesian components, $\overline{\overline{\mathbf{G}}}^0$ is the $3N \times 3N$ matrix containing the discretized free-space Green's function, and $\overline{\overline{\mathbf{G}}}$ is the $3N \times 3N$ matrix containing the unknown system Green's function. Once the system of linear equations is solved, the total radiative heat transfer coefficient, h_{rad}, is calculated as:

$$h_{\mathrm{rad}}(T) = \frac{1}{2\pi A_{\mathrm{c}}} \int_0^{\infty} \left. \frac{\partial \Theta(\omega, T')}{\partial T} \right|_{T'=T} \tau(\omega) d\omega \tag{3}$$

where $\Theta(\omega, T)$ is the mean energy of an electromagnetic state and $A_{\mathrm{c}} = Lt$ is the membrane cross-section. The spectral transmission coefficient between the two membranes of volumes V_{h} and V_{c}, denoted $\tau(\omega)$, is calculated from the system Green's function:

$$\tau(\omega) = \sum_{i \in V_{\mathrm{h}}} \sum_{j \in V_{\mathrm{c}}} 4k_0^4 \Delta V_i \Delta V_j \, \mathrm{Im}[\varepsilon(\mathbf{r}_i, \omega)] \mathrm{Im}[\varepsilon(\mathbf{r}_j, \omega)] \mathrm{Tr}[\bar{\bar{\mathbf{G}}}(\mathbf{r}_i, \mathbf{r}_j, \omega) \bar{\bar{\mathbf{G}}}^{\dagger}(\mathbf{r}_i, \mathbf{r}_j, \omega)] \tag{4}$$

where ΔV_i and ΔV_j are respectively the volumes of the i^{th} and j^{th} subvolumes used in the discretization. The spectral heat transfer coefficient shown in Fig. 3a is obtained by evaluating Eq. (3) without the integration over ω. The contribution from propagating waves to NFRHT is calculated by considering only the far-field (FF) term in the free-space Green's function (see Supplementary Section 8)[43]:

$$\bar{\bar{\mathbf{G}}}^{0,\mathrm{FF}}(\mathbf{r}, \mathbf{r}', \omega) = \frac{\exp(ik_0 r)}{4\pi r} [1 - \hat{\mathbf{r}}\hat{\mathbf{r}}^{\dagger}] \tag{5}$$

NFRHT between two infinite surfaces (Reference Case 1). The NFRHT between two SiC infinite surfaces (Reference Case 1 of Fig. 2 and Fig. 3a) is calculated using a closed-form expression derived from fluctuational electrodynamics. The propagating and evanescent components of the total radiative heat transfer coefficient are respectively calculated as[2]:

$$h_{\mathrm{rad,inf}}^{\mathrm{prop}}(T) = \frac{1}{4\pi^2} \int_0^{\infty} d\omega \left. \frac{\partial \Theta(\omega, T')}{\partial T} \right|_{T'=T} \int_0^{k_0} dk_\rho k_\rho \sum_{\gamma=TE,TM} \frac{(1-|r_{0\mathrm{h}}^{\gamma}|^2)(1-|r_{0\mathrm{c}}^{\gamma}|^2)}{|1-r_{0\mathrm{h}}^{\gamma} r_{0\mathrm{c}}^{\gamma} e^{2i\mathrm{Re}(k_{x0})d}|^2} \tag{6}$$

$$h_{\mathrm{rad,inf}}^{\mathrm{evan}}(T) = \frac{1}{\pi^2} \int_0^{\infty} d\omega \left. \frac{\partial \Theta(\omega, T')}{\partial T} \right|_{T'=T} \int_{k_0}^{\infty} dk_\rho k_\rho e^{-2\mathrm{Im}(k_{x0})d} \sum_{\gamma=TE,TM} \frac{\mathrm{Im}(r_{0\mathrm{h}}^{\gamma}) \mathrm{Im}(r_{0\mathrm{c}}^{\gamma})}{|1-r_{0\mathrm{h}}^{\gamma} r_{0\mathrm{c}}^{\gamma} e^{-2\mathrm{Im}(k_{x0})d}|^2} \tag{7}$$

where the subscripts h and c respectively refer to the hot and cold surfaces, whereas 0 denotes vacuum. In Eqs. (6) and (7), k_ρ is the wavevector parallel to the *y*-*z* plane, k_{x0} is the *x*-component of the vacuum wavevector normal to the surfaces, and $r_{0\mathrm{h}}^{\gamma}$ and $r_{0\mathrm{c}}^{\gamma}$ are respectively the Fresnel reflection coefficients at the vacuum-hot and vacuum-cold interfaces in polarization state γ. The total heat transfer coefficient reported for Reference Case 1 in Fig. 2 is the sum of Eqs. (6) and (7). Similarly, the spectral heat transfer coefficient for Reference Case 1 in Fig. 3a is the sum of Eqs. (6) and (7) without the integration over ω.

Dielectric function of polycrystalline SiC. The temperature-independent dielectric function of polycrystalline SiC is described by a Lorentz model with the parameters taken from Ref. 8:

$$\varepsilon(\omega) = \varepsilon_\infty \frac{\omega^2 - \omega_{\mathrm{LO}}^2 + i\Gamma\omega}{\omega^2 - \omega_{\mathrm{TO}}^2 + i\Gamma\omega} \tag{8}$$

where ε_∞ = 8, ω_{LO} = 1.801×10^{14} rad/s, ω_{TO} =1.486×10^{14} rad/s, and Γ = 3.767×10^{12} rad/s are respectively the high-frequency dielectric constant, the longitudinal optical phonon frequency, the transverse optical phonon frequency, and the damping constant.

Radiative heat transfer between two coplanar black membranes (Reference Case 2). The total radiative heat transfer coefficient between two membrane edges in the blackbody limit is calculated via the Stefan-Boltzmann law[40]:

$$h_{\mathrm{rad}}^{\mathrm{BB}}(T) = 4\sigma_{\mathrm{SB}} T^3 F_{12} \tag{9}$$

where σ_{SB} is the Stefan-Boltzmann constant and F_{12} is the view factor between the membrane edge face areas (treated as parallel rectangles of dimensions $L \times t$) calculated at a gap spacing d of 100 nm[40], which is the fraction of radiation energy leaving the first rectangle intercepted by the second. The view factor approaches unity when the membrane length L and thickness t are both very large compared to d ("infinite surfaces"). Note that this h_{BB} expression also explains the T^3 power law seen for Reference Case 2 in Fig. 2a, which fundamentally arises from the specific heat of photons in a 3D gray medium.

SPhP resonance of a SiC-vacuum interface. NFRHT between two infinite SiC surfaces in the deep subwavelength regime is quasi-monochromatic at the SPhP resonant frequency of a single SiC-vacuum interface. This resonant frequency, derived from a SPhP dispersion relation for a SiC-vacuum interface, can be approximated as[42]:

$$\omega_{res,inf} \approx \sqrt{\frac{\varepsilon_\infty \omega_{LO}^2 + \omega_{TO}^2}{\varepsilon_\infty + 1}} \tag{10}$$

The calculated $\omega_{res,inf}$ of 1.77×10^{14} rad/s is in excellent agreement with the maximum of the spectral heat transfer coefficient for two infinite SiC surfaces (see Fig. 3a).

Uncertainty analysis. *Theoretical predictions.* The shaded bands of theoretical predictions in Fig. 2 account for the uncertainties of the gap spacing from the SEM images as well as the tilting of the membranes from the LCM measurements. The estimated uncertainty of the gap spacing is ±10 nm. The estimated tilt angles are 0.8°, 4.8°, and 3.4° for the 120, 50, and 20 nm thick devices,

respectively (see Supplementary Section 3). The total heat transfer calculated by DSGF decreases when the membranes are tilted and when the separation gap increases. Therefore, as an example, the upper bound of the red-shaded band in Fig. 2a for the 20 nm thick device is obtained from a separate DSGF calculation assuming no tilt and by using the lower-bound estimated gap spacing of 90 nm (found by subtracting the estimated uncertainty of 10 nm from the nominal gap spacing of 100 nm). Similarly, the lower bound of the red-shaded band comes from another DSGF calculation using the full tilting of 3.4° and by assuming an upper-bound gap of 110 nm. The same procedure is used to calculate the theoretical curves for the 50 and 120 nm thick devices, each based on their respective estimated gap spacings, tilts, and uncertainties thereof. Note that the effects of tilting on NFRHT between the SiC membranes are small; for example, h_{rad} decreases by only 11% for the maximum tilt angle of 4.8° in the 50 nm thick device.

In addition, the 120, 50, and 20 nm thick SiC membranes may be misaligned by respectively 20, 10, and 10 nm along the y-direction according to the LCM line scans (see Supplementary Section 3). DSGF simulations show that such misalignments have a negligible impact on the total radiative heat transfer, such that they are not included in the uncertainty analysis. For example, h_{rad} decreases by less than 1% when the 20 nm thick membranes are misaligned by 10 nm in y.

Experimental data. The estimated uncertainty of the measured heat transfer coefficients in Fig. 2 is ±10% (representing a 68% confidence interval), which comes from the uncertainties of the membrane dimensions and in the resistance thermometry of the PRTs. The lengths and thicknesses, respectively, of the membranes are determined using a Zeiss SEM and a spectroscopic ellipsometer (Angstrom Sun Technologies model SE200BM), both with uncertainties estimated as 2% or better

(see also Ref. 34). The uncertainties in the resistance thermometry are typically 5% or less of the relevant ΔT (see Supplementary Sections 5 and 6).

Data availability. The data that support the findings of this study are available from the corresponding authors on request.

Code availability. The code used to calculate near-field radiative heat transfer between membranes based on the discrete system Green's function method has been deposited on Zedono (DOI: 10.5281/zenodo.10515348).

Acknowledgments. L.T. and C.D. gratefully acknowledge financial support from the Marjorie Jackson Endowed Fellowship Fund, the Howard Penn Brown Chair, and the Army Research Laboratory as part of the Collaborative for Hierarchical Agile and Responsive Materials (CHARM) under Cooperative Agreement No. W911NF-19-2-0119. L.M.C. and M.F. acknowledge the financial support from the National Science Foundation (grant number CBET-1952210) and from the Natural Sciences and Engineering Research Council of Canada (funding reference number RGPIN-2023-03513). This work was partially performed at the UC Berkeley Marvell Nanolab. The authors appreciate the support of the staff and facilities that made this work possible. This research used the Savio computational cluster resource provided by the Berkeley Research Computing program at the University of California, Berkeley (supported by the UC Berkeley Chancellor, Vice Chancellor for Research, and Chief Information Officer).

Author contributions. This work was initialized and conceived by L.T. Design, fabrication and testing of the devices were performed by L.T. under the supervision of C.D. Numerical simulations were performed by L.T. with help of L.M.C. under the supervision of M.F. All authors contributed to the data analysis. The manuscript was written by L.T., M.F. and C.D.

Competing interests. The authors declare no competing interests.

References

1. Planck, M. The Theory of Heat Radiation [transl. Masius, M.] (P. Blakiston's Son & Co., Philadelphia, 1914).

2. Mulet, J. P., Joulain, K., Carminati, R., & Greffet, J. J. Enhanced radiative heat transfer at nanometric distances. Microscale Thermophysical Engineering 6, 209-222 (2002).

3. Joulain, K., Mulet, J. P., Marquier, F., Carminati, R., & Greffet, J. J. Surface electromagnetic waves thermally excited: Radiative heat transfer, coherence properties and Casimir forces revisited in the near field. Surface Science Reports 57, 59-112 (2005).

4. Rousseau, E., Laroche, M., & Greffet, J. J. Radiative heat transfer at nanoscale: Closed-form expression for silicon at different doping levels. Journal of Quantitative Spectroscopy and Radiative Transfer 111, 1005-1014 (2010).

5. Song, B., Thompson, D., Fiorino, A., Ganjeh, Y., Reddy, P., & Meyhofer, E. Radiative heat conductances between dielectric and metallic parallel plates with nanoscale gaps. Nature Nanotechnology 11, 509-514 (2016).

6. Lim, M., Song, J., Lee, S. S., & Lee, B. J. Tailoring near-field thermal radiation between metallo-dielectric multilayers using coupled surface plasmon polaritons. Nature Communications 9, 4302 (2018).

7. DeSutter, J., Tang, L., & Francoeur, M. A near-field radiative heat transfer device. Nature Nanotechnology 14, 751-755 (2019).

8. St-Gelais, R., Zhu, L., Fan, S., & Lipson, M. Near-field radiative heat transfer between parallel structures in the deep subwavelength regime. Nature Nanotechnology 11, 515-519 (2016).

9. Luo, X. et al. Observation of Near-Field Thermal Radiation between Coplanar Nanodevices with Subwavelength Dimensions. Nano Letters 24, 1502-1509 (2024).

10. Berini, P. Plasmon–polariton modes guided by a metal film of finite width. Optics Letters 24, 1011-1013 (1999).

11. Berini, P. Plasmon-polariton waves guided by thin lossy metal films of finite width: Bound modes of symmetric structures. Physical Review B 61, 10484 (2000).

12. Salihoglu, H. et al. Near-field thermal radiation between two plates with sub-10 nm vacuum separation. Nano Letters 20, 6091-6096 (2020).

13. Mittapally, R., Lim, J. W., Zhang, L., Miller, O. D., Reddy, P., & Meyhofer, E. Probing the limits to near-field heat transfer enhancements in phonon-polaritonic materials. Nano Letters 23, 2187-2194 (2023).

14. Ito, K., Miura, A., Iizuka, H. & Toshiyoshi, H. Parallel-plate submicron gap formed by micromachined low-density pillars for near-field radiative heat transfer. Applied Physics Letters 106, 083504 (2015).

15. Watjen, J. I., Zhao, B. & Zhang, Z. M. Near-field radiative heat transfer between doped-Si parallel plates separated by a spacing down to 200 nm. Applied Physics Letters 109, 203112 (2016).

16. Ghashami, M. et al. Precision measurement of phonon-polaritonic near-field energy transfer between macroscale planar structures under large thermal gradients. Physical Review Letters 120, 175901 (2018).

17. Tang, L., DeSutter, J., & Francoeur, M. Near-field radiative heat transfer between dissimilar materials mediated by coupled surface phonon-and plasmon-polaritons. ACS Photonics 7, 1304-1311 (2020).

18. Ying, X., Sabbaghi, P., Sluder, N., & Wang, L. Super-planckian radiative heat transfer between macroscale surfaces with vacuum gaps down to 190 nm directly created by SU-8 posts and characterized by capacitance method. ACS Photonics 7, 190-196 (2019).

19. Polder, D. V. H. M., & Van Hove, M. Theory of radiative heat transfer between closely spaced bodies. Physical Review B 4, 3303 (1971).

20. Rytov, S. M., Kravtsov, Y. A., Tatarskii, V. I. Principles of Statistical Radiophysics; Springer: New York, 1989.

21. Lussange, J., Guérout, R., Rosa, F. S., Greffet, J. J., Lambrecht, A., & Reynaud, S. Radiative heat transfer between two dielectric nanogratings in the scattering approach. Physical Review B 86, 085432 (2012).

22. Guha, B., Otey, C., Poitras, C. B., Fan, S., & Lipson, M. Near-field radiative cooling of nanostructures. Nano Letters 12, 4546-4550 (2012).

23. Ito, K., Nishikawa, K., Miura, A., Toshiyoshi, H., & Iizuka, H. Dynamic modulation of radiative heat transfer beyond the blackbody limit. Nano Letters 17, 4347-4353 (2017).

24. Lang, S. et al. Dynamic measurement of near-field radiative heat transfer. Scientific Reports 7, 13916 (2017).

25. Fiorino, A. et al. A thermal diode based on nanoscale thermal radiation. ACS Nano 12, 5774-5779 (2018).

26. Zhu, L., Fiorino, A., Thompson, D., Mittapally, R., Meyhofer, E., & Reddy, P. Near-field photonic cooling through control of the chemical potential of photons. Nature 566, 239-244 (2019).

27. Shi, K., Chen, Z., Xing, Y., Yang, J., Xu, X., Evans, J. S., & He, S. Near-field radiative heat transfer modulation with an ultrahigh dynamic range through mode mismatching. Nano Letters 22, 7753-7760 (2022).

28. Fiorino, A., Zhu, L., Thompson, D., Mittapally, R., Reddy, P., & Meyhofer, E. Nanogap near-field thermophotovoltaics. Nature Nanotechnology 13, 806-811 (2018).

29. Inoue, T., Koyama, T., Kang, D. D., Ikeda, K., Asano, T., & Noda, S. One-chip near-field thermophotovoltaic device integrating a thin-film thermal emitter and photovoltaic cell. Nano Letters 19, 3948-3952 (2019).

30. Bhatt, G. R. et al. Integrated near-field thermo-photovoltaics for heat recycling. Nature Communications 11, 2545 (2020).

31. Lucchesi, C., Cakiroglu, D., Perez, J. P., Taliercio, T., Tournié, E., Chapuis, P. O., & Vaillon, R. Near-field thermophotovoltaic conversion with high electrical power density and cell efficiency above 14%. Nano Letters 21, 4524-4529 (2021).

32. Mittapally, R. et al. Near-field thermophotovoltaics for efficient heat to electricity conversion at high power density. Nature Communications 12, 4364 (2021).

33. Walter, L. P., Tervo, E. J., & Francoeur, M. Near-field radiative heat transfer between irregularly shaped dielectric particles modeled with the discrete system Green's function method. Physical Review B 106, 195417 (2022).

34. Tang, L., & Dames, C. Effects of thermal annealing on thermal conductivity of LPCVD silicon carbide thin films. Journal of Applied Physics 134, 165101 (2023).

35. Li, D., Wu, Y., Kim, P., Shi, L., Yang, P., & Majumdar, A. Thermal conductivity of individual silicon nanowires. Applied Physics Letters 83, 2934-2936 (2003).

36. Shi, L. et al. Measuring thermal and thermoelectric properties of one-dimensional nanostructures using a microfabricated device. Journal of Heat Transfer 125, 881-888 (2003).

37. Sadat, S., Chua, Y. J., Lee, W., Ganjeh, Y., Kurabayashi, K., Meyhofer, E., & Reddy, P. Room temperature picowatt-resolution calorimetry. Applied Physics Letters 99, 043106 (2011).

38. Sadat, S., Meyhofer, E., & Reddy, P. Resistance thermometry-based picowatt-resolution heat-flow calorimeter. Applied Physics Letters 102, 163110 (2013).

39. Thompson, D. et al. Hundred-fold enhancement in far-field radiative heat transfer over the blackbody limit. Nature 561, 216-221 (2018).

40. Modest, M. F. Radiative Heat Transfer 3rd edn (Academic Press, New York, 2013).

41. Archambault, A., Teperik, T. V., Marquier, F., & Greffet, J. J. Surface plasmon Fourier optics. Physical Review B 79, 195414 (2009).

42. Francoeur, M., Mengüç, M. P., & Vaillon, R. Spectral tuning of near-field radiative heat flux between two thin silicon carbide films. Journal of Physics D: Applied Physics 43, 075501 (2010).

43. Novotny, L., & Hecht, B. Principles of nano-optics. Cambridge University Press (2012).

Extended Data

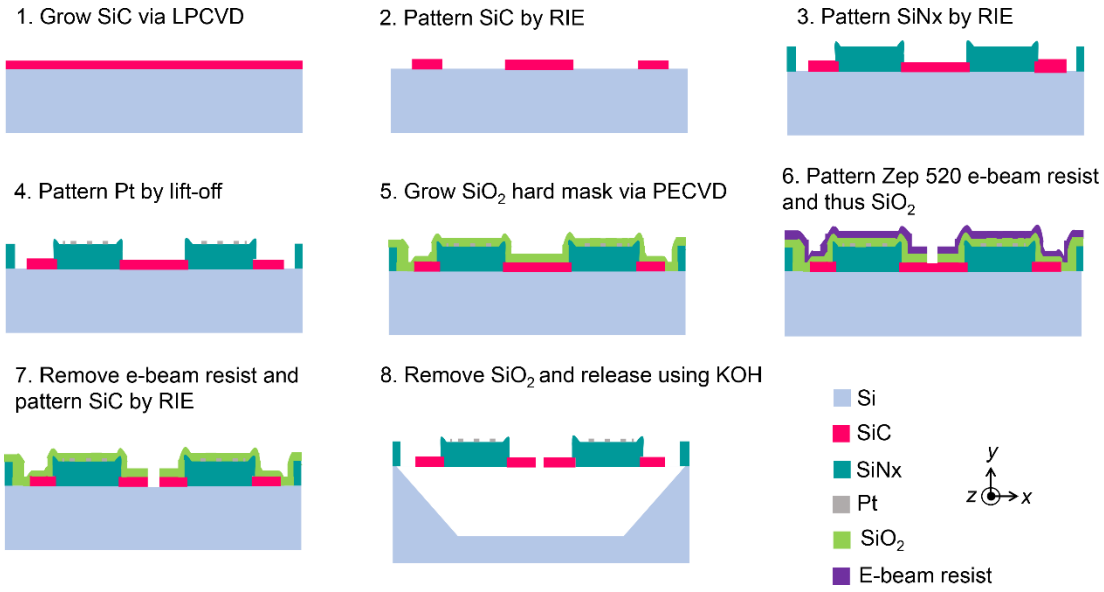

Extended Data Fig. 1 | Device fabrication. Main steps for fabricating the suspended devices used for measuring NFRHT between two SiC membranes. More information is given in Supplementary Section 1.

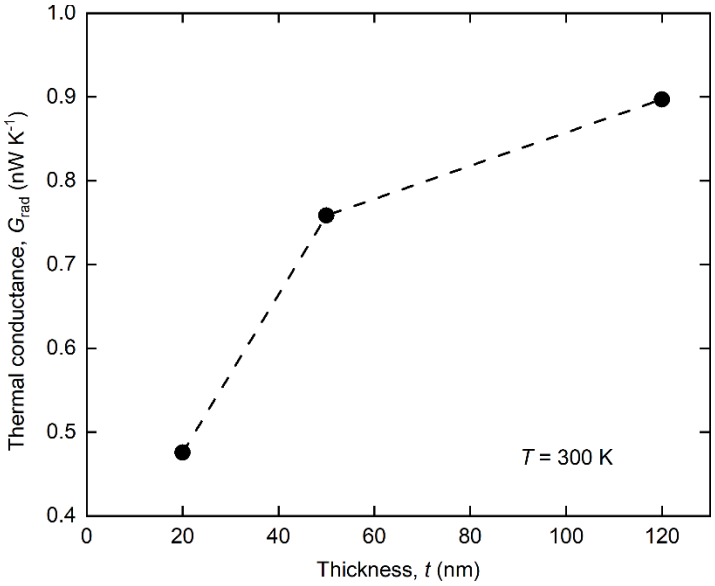

Extended Data Fig. 2 | DSGF calculated thermal conductance G_{rad} at 300 K between two 120, 50, and 20 nm thick SiC membranes separated by a vacuum gap d = 100 nm. The results correspond to those shown in Fig. 3a after integrating over all frequencies ω and multiplying by t and L.

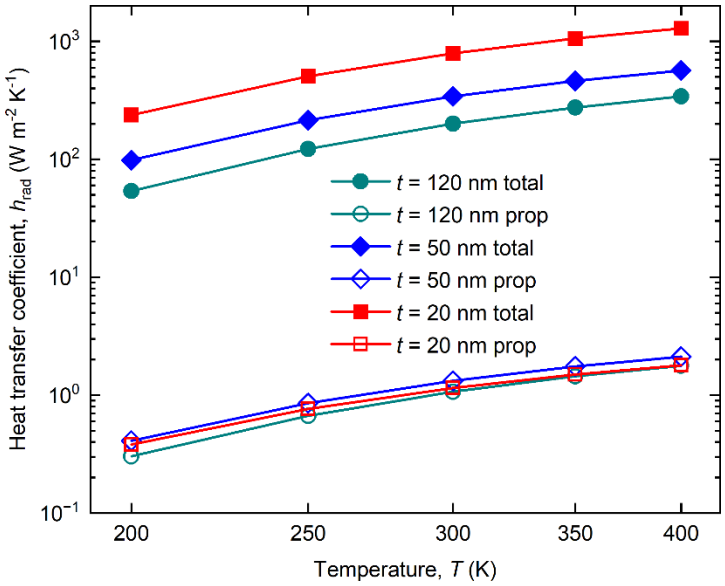

Extended Data Fig. 3 | DSGF calculated contributions from propagating waves to NFRHT between two SiC membranes, using the gaps *d* given in Supplementary Table 1. The heat transfer coefficient due to propagating (prop) waves is plotted in hollow points. The total heat transfer coefficient, accounting for both propagating and evanescent waves, is also included for comparison as solid points (the results correspond to the case where the nominal values of the gap sizes are used and the tilts are not considered, or roughly the middle of the theoretical bands as shown in Fig. 2 of the main text). Propagating waves account for less than 1% of the total heat transfer for all temperatures and membrane thicknesses.

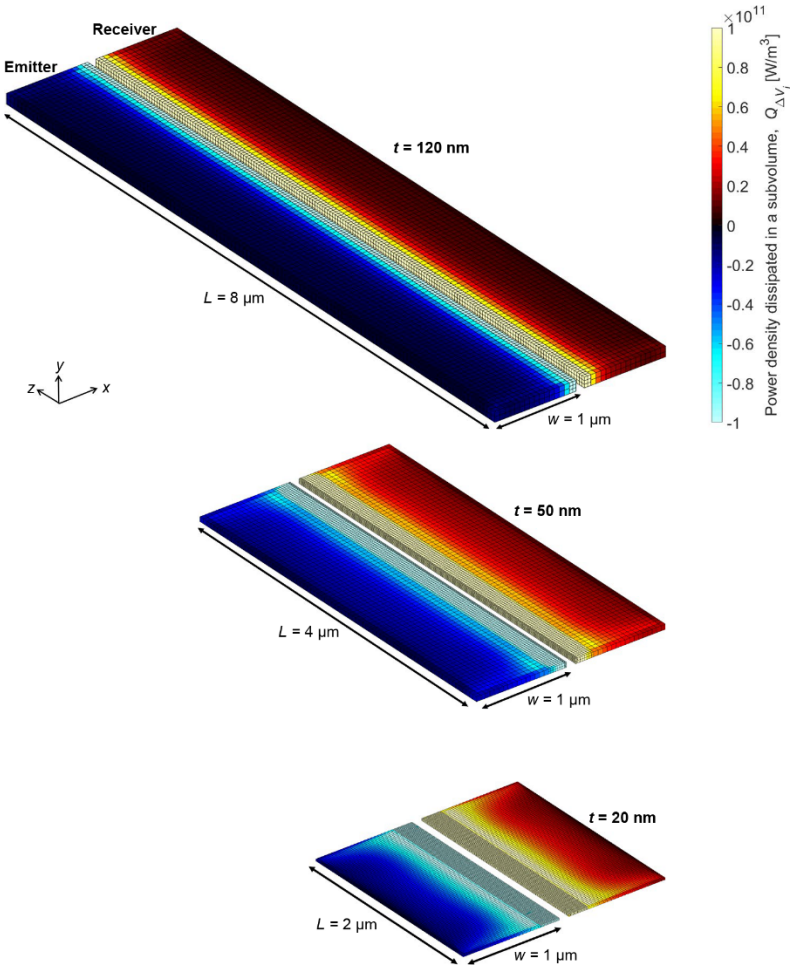

Extended Data Fig. 4 | DSGF calculations of the spatial distribution of power density dissipated at 300 K between two 120, 50, and 20 nm thick SiC membranes separated by a vacuum gap d = 100 nm. Positive and negative values of the color bar represent heat gain and heat loss, respectively. The simulations are respectively performed for L values of 8, 4, and 2 μm for 120, 50, and 20 nm thick membranes, all with w = 1 μm to obtain converged results (see Supplementary Section 7 for more details on the convergence of DSGF simulations).